Flow patterns in a steady lid-driven rectangular cavity with an embedded circular cylinder

Jianxun Zhu,[1, a)] Lars Erik Holmedal,[1] Hong Wang,[1] and Dag Myrhaug[1]
1. Department of Marine Technology, Norwegian University of Science and Technology, Trondheim, Norway

(Dated: 8 April 2021)

A detailed investigation of the flow in a steady lid-driven cavity of depth to width ratio 1:2 containing a circular cylinder is provided. Three different Reynolds numbers (based on the lid velocity and cavity depth) of 100, 500 and 1000 as well as four different cylinder radius to cavity depth ratios (0.1, 0.2, 0.3 and 0.4) located at three different positions along the horizontal centerline of the cavity, are considered. It appears that these flows can be classified into seven different flow patterns. These flow patterns are given for different cylinder radii and positions as well as Reynolds numbers. There is a tendency that for a given cylinder radius, there are more transitions between different flow patterns for a small radius than for a large radius while for a given Reynolds number, the number of transitions is larger for high Reynolds numbers than for low Reynolds numbers. Overall, a larger number of flow patterns tend to emerge as the Reynolds number increases for small radii. The largest variety of flow patterns occur for the left-sided cylinder due to the interaction with the large anti-clockwise circulation flow formed at the bottom left corner.

Keywords: Immersed boundary method; lid-driven cavity; embedded cylinder; vortex structures; laminar flow.

[a)]Corresponding author: jianxun.zhu@ntnu.no

NOMENCLATURE

Γ	Immersed boundary
λ_x, λ_y	Directional weighting factors
ν	Fluid kinematic viscosity
Φ	Pressure correction
ρ	Fluid density
C_p	Pressure coefficient
D	Cylinder diameter
H	Cavity height
p	Pressure
p_0	Pressure at the bottom left corner
r	Cylinder radius
Re	Reynolds number
t	Time
U	Lid-driven velocity
U_0	Free-stream velocity
u_i	Fluid velocity
u_i^*	Tentative velocity
x, y	Cartesian coordinates

I. INTRODUCTION

Steady lid-driven flows containing a solid body have gained considerable attention due to its engineering applications in heat exchangers and electric coolers. The presence of a solid body within the cavity such as a circular[1,2] or square[3] cylinder changes the flow patterns substantially, forming strong vortices which are not present in the absence of the solid body. This might strongly affect e.g. mixing or cooling properties of the cavity since these vortices might cause large gaps between isotherms, thus affecting the heat transfer within the cavity. For an incompressible fluid, the effect of moderate temperature gradients on the flow might be small, i.e. the Richardson

number is small. In this case the flow is dominated by momentum and the flow structures are nearly independent of the temperature field.

Oztop et al.[1] and Khanafer and Aithal[2] investigated mixed convection and heat transfer in a steady lid-driven square cavity containing a circular cylinder by using a finite volume method and a finite element formulation, respectively. Oztop et al.[1] showed that changing the the cylinder position and radius leads to deformation of both the streamlines and the isotherms in the cavity, although the primary and bottom corner vortices were not investigated in detail. The deformation of the primary vortex caused by the cylinder radius and the temperature field has been investigated numerically by Khanafer and Aithal[2] who found that for a low Richardson number of 0.01 (forced convection flow), a primary vortex is formed between the moving lid and the centered circular cylinder, and that an increase in the cylinder radius leads to the primary vortex breaking up into two vortices. As the Richardson number increases, these vortices shrink gradually and disappear due to the natural (thermal) convection. Similar results were obtained by Billah et al.[4].

Galaktionov et al.[5] developed an analytical method to study creeping flow in a steady-lid driven rectangular cavity with a centered fixed and rotating circular cylinder. As the upper lid moves towards the right for the fixed cylinder, they found that the flow is symmetric about the vertical centerline of the cavity with two clockwise vortices attached to the upper left and the upper right sides of the cylinder.

Khanafer et al.[6] used a finite element formulation to investigate the mixed convection in a lid-driven square cavity with two circular cylinders. These two cylinders are placed symmetrically about the vertical centerline of the cavity. They found that, for low Richardson numbers, an elongated clockwise vortex was formed between the lid and the two cylinders. As these two cylinders move closer to the bottom, this elongated vortex increases in size. As the two cylinders move closer to the lid, the vortex appears to be split into three clockwise vortices located beneath the mid of the lid as well as at the upper left and right corners, respectively.

The hydro-magnetic mixed convection in a steady lid-driven square cavity with a heat-conducting circular cylinder was investigated by Chatterjee and Gupta[7] as well as Ray and Chatterjee[8] who also studied the effect of corner heaters with Joule heating. The mixed convection for nanofluids in a steady lid-driven square cavity with embedded circular cylinders was investigated by Chatterjee et al.[9], Bansal and Chatterjee[10] as well as Chatterjee and Halder[11].

Billah et al.[4] and Khanafer and Aithal[2] investigated the effect of the cylinder radius on the primary vortex for flow within a steady lid-driven square cavity with an embedded cylinder. However, a detailed investigation of the flow structures (including the primary vortex, corner and bottom vortices as well as the pressure around the circular cylinder) has not been previously presented. The aim of the present work is to present such detailed results for very low Richardson numbers, where the effect of the temperature field is negligible. Moreover, the effect of increasing the cavity aspect ratio on this flow has not been investigated previously.

Specifically, a detailed investigation of the flow structures within a lid-driven cavity of height to length ratio 1:2 containing a circular cylinder are conducted for a range of Reynolds numbers (based on the lid velocity and the cavity height), cylinder radius to cavity height ratio, for left-, right- and mid-centered cylinders are provided. Numerical simulations show that this flow can be classified into seven different flow patterns which are here visualized by streamlines. These flow patterns are unique functions of the Reynolds number, the ratio between the cylinder radius and

the cavity height, as well as the position of the cylinder within the cavity.

II. NUMERICAL METHOD

A. Basic numerical scheme

Incompressible flow with a constant density ρ and kinematic viscosity ν is governed by the two-dimensional Navier-Stokes equations described as follows

$$\frac{\partial u_i}{\partial x_i} = 0 \tag{1}$$

$$\frac{\partial u_i}{\partial t} + \frac{\partial u_i u_j}{\partial x_j} = -\frac{\partial p}{\partial x_i} + \frac{1}{Re}\frac{\partial^2 u_i}{\partial x_j \partial x_j} \tag{2}$$

where the Einstein notation using repeated indices is applied. Here u_i = (u,v) and x_i = (x, y) for i = 1 and 2, are the velocity and Cartesian coordinates, respectively, whilst t, p and $Re = UH/\nu$ denote the dimensionless time, dimensionless pressure and Reynolds number, respectively, where H is the depth of cavity and U is the lid motion velocity. The time, pressure and length are scaled by H/U, ρU^2 and H, respectively.

Equations (1) and (2) are discretized on a staggered mesh arrangement using second-order central differences. A projection method using a second-order Adams-Bashforth scheme for the convective terms and a Crank-Nicolson scheme for the diffusive terms is applied. The intermediate velocity u_i^* is obtained as

$$u_i^* = u_i^n + \Delta t[\frac{1}{2}(3H_i^n - H_i^{n-1}) + \frac{1}{2}(F_i^n + F_i^*) - \frac{\delta}{\delta x_i}(p^{n-1:2})] \tag{3}$$

where $\delta/\delta x_i$ represents the numerical spatial gradient operator; the convective and diffusive terms are denoted by $H_i = \delta(u_i u_j)/\delta x_j$ and $F_i = \nu\delta^2(u_i)/(\delta x_j \delta x_j)$, respectively; the superscript n denotes the time step, and $p^{n-1:2}$ is the pressure obtained at the previous time-step. The velocity correction is given as

$$u_i^{n+1} = u_i^* - \Delta t\frac{\delta}{\delta x_j}(\phi^{n+1}) \tag{4}$$

where $\phi^{n+1} = p^{n+1:2} - p^{n-1:2}$ is determined such that the resulting velocity field u_i^{n+1} satisfies the continuity condition. Substitution of equation (4) into the continuity equation $\delta u_i/\delta x_i = 0$ yields a Poisson equation for the pressure correction

$$\frac{\delta^2}{\delta x_j^2}(\phi^{n+1}) = -\frac{1}{\Delta t}\frac{\delta u_i^*}{\delta x_i} \tag{5}$$

which is solved using a Jacobi preconditioned bi-conjugate gradient stabilized method.

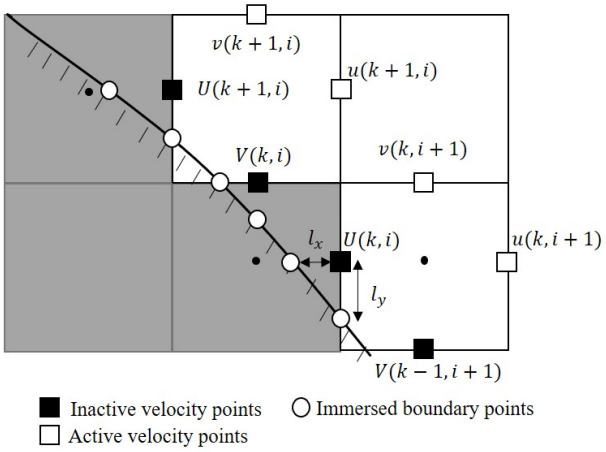

FIG. 1. Definition of the inactive velocity points (■), immersed boundary points (◯), and active velocity points (□).

B. Implementation of the immersed boundary method

The immersed boundary technique is based on a direct forcing approach combined with a finite difference method firstly proposed by Fadlun et al.[12]. The application of this technique is due to memory and CPU savings and easy grid generation compared to the unstructured grid method. As shown in figure 1, the staggered velocity components nearest the immersed boundary are set as inactive velocity points (■) which are updated by interpolation. Here, a one-dimensional, linear interpolation scheme is applied in each direction according to the following stencil formulation

$$u_i = \frac{x_i - x_\Gamma}{x_{i+1} - x_\Gamma} u_{i+1} + \frac{x_{i+1} - x_i}{x_{i+1} - x_\Gamma} u_\Gamma, \quad i = 1,2 \tag{6}$$

where u_Γ and x_Γ are the velocity and position of the immersed boundary, respectively.

If an inactive velocity point can be interpolated from two directions, each direction is multiplied by a weighting factor as follows[13,14]

$$u_i = \lambda_x u_i^x + \lambda_y u_i^y \tag{7}$$

where the superscript x and y denotes the interpolation in x and y-directions, respectively, and the weighting factors λ_x and λ_y are given as

$$\lambda_x = \frac{1}{1 + (\frac{l_x}{l_y})^2} \quad and \quad \lambda_y = \frac{1}{1 + (\frac{l_y}{l_x})^2} \tag{8}$$

where l_x and l_y is the distance between the inactive velocity point and the immersed boundary in x and y-directions, respectively, as shown in figure 1. A Neumann condition is applied for the pressure correction at the inactive velocity points.

III. RESULTS AND DISCUSSION

A. Uniform flow past a free circular cylinder at $Re' = 40$

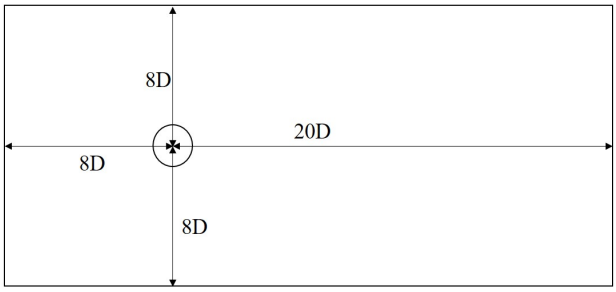

FIG. 2. Computation domain for flow past a free circular cylinder.

Two-dimensional flow past a circular cylinder has been investigated using the present method for a Reynolds number ($Re' = U_0 D/\nu$, where D is the diameter of cylinder and U_0 is free-stream velocity) equal to 40. The dimensionless free-stream velocity U_0 = 1 is specified at the inlet boundary while a Neumann condition is imposed on the velocity at the outlet and at the top and bottom of the flow domain. Non-slip conditions are applied on the cylinder. The pressure is set to be zero at the outlet and a Neumann condition for the pressure correction is used at the other boundaries. Figure 2 shows the computation domain where the inlet and lateral boundaries are located 8D upstream of the cylinder and the outlet is located at 20D downstream of the cylinder. A uniform mesh of size 0.02D is employed for this domain.

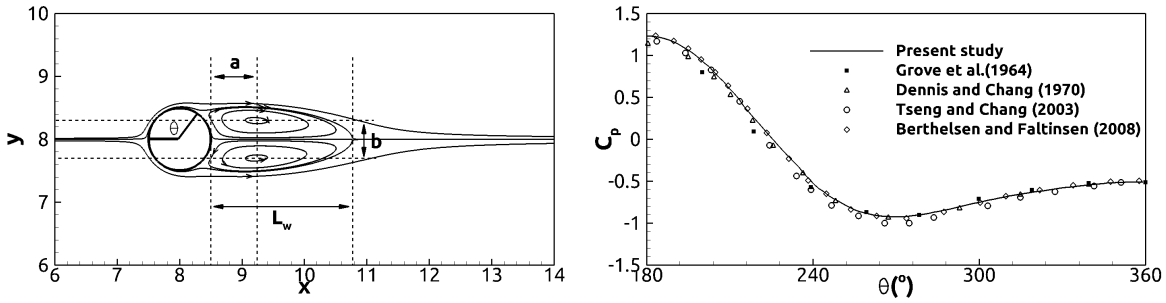

FIG. 3. Left image: streamlines for the flow over a cylinder at $Re' = 40$ and nomenclature used in Table I; separation angle θ, wake length L_w, horizontal distance a between the rear stagnation point of the cylinder and the recirculation center and vertical distance b between the symmetric recirculation centers; right image: comparison between the present and previous results for the pressure coefficient (C_p) on the bottom half of the cylinder surface at $Re' = 40$. The upstream stagnation point is located at $\theta = 180^\circ$.

After a spin-up time of $t = t^* U_0/D = 200$ (where t^* is the physical time), the flow reaches a steady and symmetric state where two attached recirculating vortices are formed behind the cylinder. The streamlines for the flow past the cylinder at $Re' = 40$, as well as the separation angle θ, wake length L_w, the horizontal distance a between the rear stagnation point of the cylinder and the

	C_D	θ	L_w	a	b
Tseng and Ferziger[15]	1.53		2.21		
Coutanceau and Bouard[16]		126.2°	2.13	0.76	0.59
Bounchon et al.[17]	1.50	126.6°	2.26	0.71	0.60
Gautier et al.[18]	1.49	126.4°	2.24	0.71	0.59
Fornberg[19]	1.50	124.4°	2.24		
Patil and Lakshmisa[20]	1.56	127.3°	2.14		
Present study	1.56	126.8°	2.27	0.74	0.60

TABLE I. The physical parameters obtained by the present numerical method and previous works for the flow past a circular cylinder at $Re' = 40$.

recirculation center and vertical distance b between the symmetric recirculation centers, are shown in figure 3. Here the characteristic wake dimensions L_w, a and b are scaled by D. The pressure coefficient ($C_p = \frac{p-p_\infty}{0.5\rho U_0^2}$, where p_∞ is the pressure at the outlet) along the bottom half boundary of the cylinder is presented in figure 3, showing a good agreement with both experimental[21] and numerical[14,15,22] results. The characteristic wake dimensions L_w, a and b as well as the drag coefficient (C_D) are given in table I. The predicted separation angle θ and wake length L_w compare well with the experimental results obtained by Coutanceau and Bouard[16] while the predicted distance a is smaller than their measurements, but in good agreement with the numerical results obtained by Bounchon et al.[17] and Gautier et al..[18] Moreover, a good agreement for the drag coefficient is obtained by comparison with previously numerical predictions[15,17–20] as shown in table I.

B. Flow in a steady lid-driven square cavity with an embedded cylinder

The vortex structures in a steady lid-driven square cavity with a centered cylinder have been investigated for Reynolds numbers ($Re = UH/\nu$) equal to 100, 500 and 1000. Moreover, two cylinders of dimensionless radius $r = r'/H = 0.2$ and 0.3 are considered.

Figure 4 shows the velocity components u and v along $x = 0.5$ and $y = 0.5$, respectively, for the steady lid-driven cavity containing a centered cylinder of $r = 0.2$ for $Re = 1000$. A coarse mesh of $\Delta x = \Delta y = 0.01$ and a fine mesh of $\Delta x = \Delta y = 0.005$ are used to obtain the present results, which are in good agreement with those given by Cai et al..[23] It appears that the coarse mesh is sufficient to obtain grid independent results.

Figure 5 shows the streamline contours within a steady lid-driven square cavity with a centered cylinder of $r = 0.2$ (left column) and 0.3 (right column). For the smallest cylinder (left column), the lid-driven flow rolls up at the upper boundary of the cylinder, forming an elongated clockwise primary vortex while flow separation and reattachment at the bottom corner induce two weak anti-clockwise bottom corner vortices which are also present in the absence of the cylinder[24]. As Re increases from 100 to 1000 (left column), the primary vortex decreases in size and moves closer towards the cylinder while the bottom corner vortices grow in size and strength. For the largest cylinder (at $Re = 100$; right column), it appears that the primary vortex breaks up into two

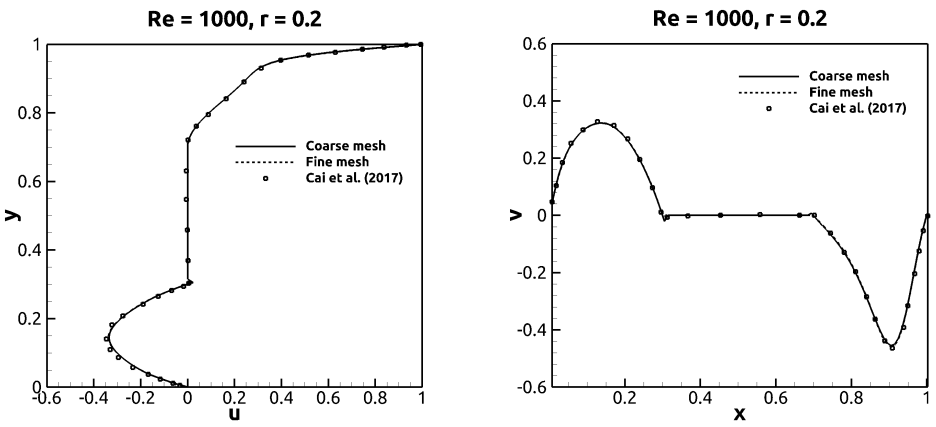

FIG. 4. Comparison of the velocity profiles for steady lid-driven square cavity flow containing a centered cylinder of $r = 0.2$ for $Re = 1000$ obtained by the present method and by Cai et al.[23]: left image, distribution of the horizontal velocity component u along $x = 0.5$; right image, distribution of the vertical velocity component v along $y = 0.5$.

clockwise vortices. These patterns were previously predicted by Khanafer and Aithal[2] for the same Re, size and position of the cylinder for a low Richardson number $R_i = 0.01$, implying that the flow is dominated by momentum instead of temperature gradients and consequently that this prediction is comparable with the present one where the effect of temperature gradients is neglected. Here $R_i = Gr/Re^2$, where $Gr = \frac{g\beta(T_h - T_c)H^3}{\nu^2}$; g is the acceleration due to gravity; β is the thermal expansion coefficient; T_h and T_c are the temperatures of the hot and cold walls, respectively). As Re increases to 1000 (right column), only one primary vortex is present both for $r = 0.2$ and 0.3, indicating that the size of cylinder is a key parameter for the break-up of the primary vortex. Moreover, increasing the cylinder size leads to a weaker primary vortex core as well as weaker bottom corner vortices.

C. Flow patterns in a steady lid-driven rectangular cavity with an embedded cylinder

A detailed investigation of the flow within the steady lid-driven cavity of height to length ratio AR = 1:2 containing a circular cylinder has been conducted for Re = 100, 500 and 1000. These three values are the classic values for the laminar mixed convection flow in a lid-driven cavity flow with an embedded body.[1–3] Three different locations, i.e. (x, y) = (0.5, 0.5), (1, 0.5) and (1.5, 0.5), as well as four different cylinder radii (r = 0.1, 0.2, 0.3 and 0.4) are considered using a resolution of 200x100 uniform grid cells which is sufficient for obtaining grid independent results. Flow in a steady lid-driven cavity of AR = 1:2 without the cylinder is given as a reference in figure 6 for Re = 100, 500 and 1000. These results are in good agreement with previous results by Cheng et al.[24], showing that the cavity contains a clockwise primary vortex as well as two anti-clockwise bottom corner vorticies. It is shown that an increase in Re leads to a noticeable growth of the bottom left corner vortex. Further validations for pure lid-driven cavity flows are given in Zhu et al.[25].

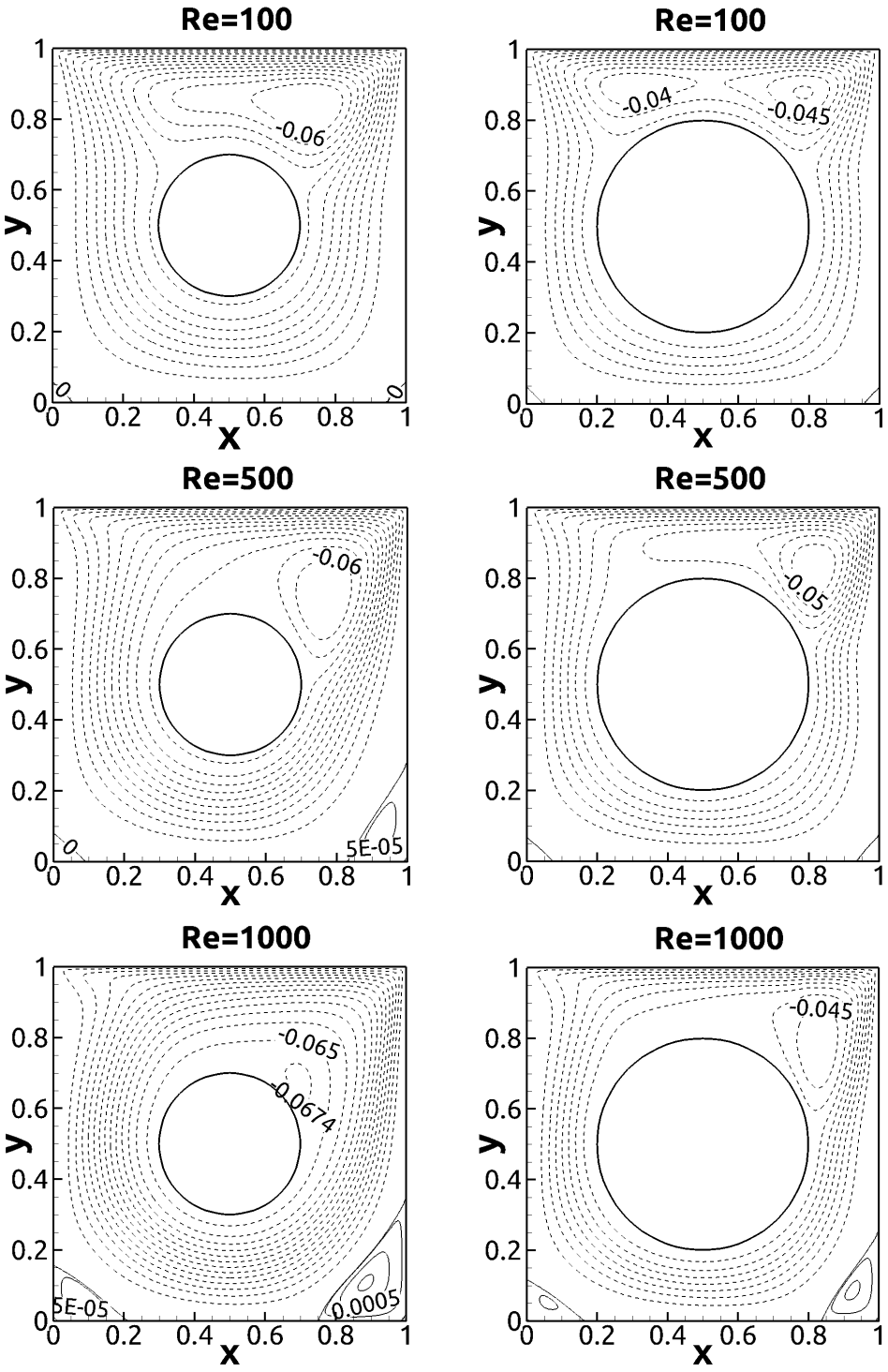

FIG. 5. Streamline contours for the flow in a steady lid-driven square cavity with a centered cylinder of r = 0.2 (left column) and 0.3 (right column) for Re = 100, 500 and 1000. Solid and dashed lines denote the positive and negative contour values, respectively; for the streamline contours, the equal difference in value of 0.005 between the two unmarked adjacent contour lines is used.

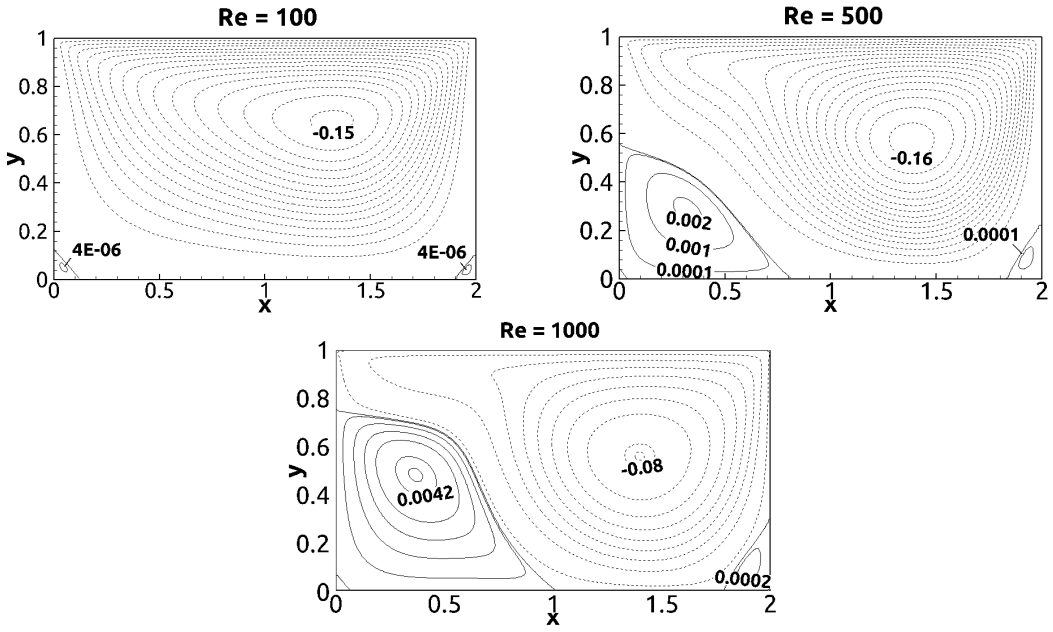

FIG. 6. Streamline contours for flow in a steady lid-driven cavity of AR = 1:2 without the cylinder for Re = 100, 500 and 1000.

1. Left-centered cylinder

Figure 7 shows streamline contours for flow in a steady lid-driven cavity of AR = 1:2 containing a cylinder located at (0.5, 0.5) for r = 0.1, 0.2, 0.3 and 0.4 with Re = 100. For r = 0.1, the cavity contains a clockwise primary vortex to the right of the cylinder and two anti-clockwise bottom corner vortices. This flow denotes the flow pattern *I* which remains qualitatively the same for r = 0.2. As r increases further to 0.3, the blockage effect between the lid and the cylinder top increases, leading to the flow rolling down at the upper-left boundary of the cylinder, thus forming a new clockwise vortex; this is also present for r = 0.4. This flow pattern is denoted *II*. Increasing r from 0.1 to 0.4 leads to a weakening of the primary vortex to the right of the cylinder while the bottom corner vortices are only weakly affected. This is due to the decreased space between the left wall and the cylinder impeding the growth of the primary vortex.

Figure 8 shows streamline contours for the same geometry as in figure 7 for Re = 500. For r = 0.1, there is a large clockwise primary vortex to the right of the cylinder while the flow circulates anti-clockwisely around the cylinder. This is due to the growth of the bottom left corner vortex (as Re increases) which also exists in a steady lid-driven cavity of the same AR without the cylinder as shown in figure 6 (see also Cheng and Hung[24], 2006; figure 3). The flow in this circulation region rolls up at the upper left side of the cylinder and down at the lower right side of the cylinder, forming two anti-clockwise vortices. This flow is denoted flow pattern *III*. As r increases to 0.2, the decreasing gap between the cylinder and the adjacent walls leads to a larger velocity there, destroying the anti-clockwise flow circulation region shown for r = 0.1. Instead, a bottom vortex is formed. This flow pattern is denoted *IV* and remains the same as r increases to 0.3 but with a smaller bottom vortex than for r = 0.2. For r = 0.4, this bottom vortex vanishes, and the flow here is thus exhibiting flow pattern *II*.

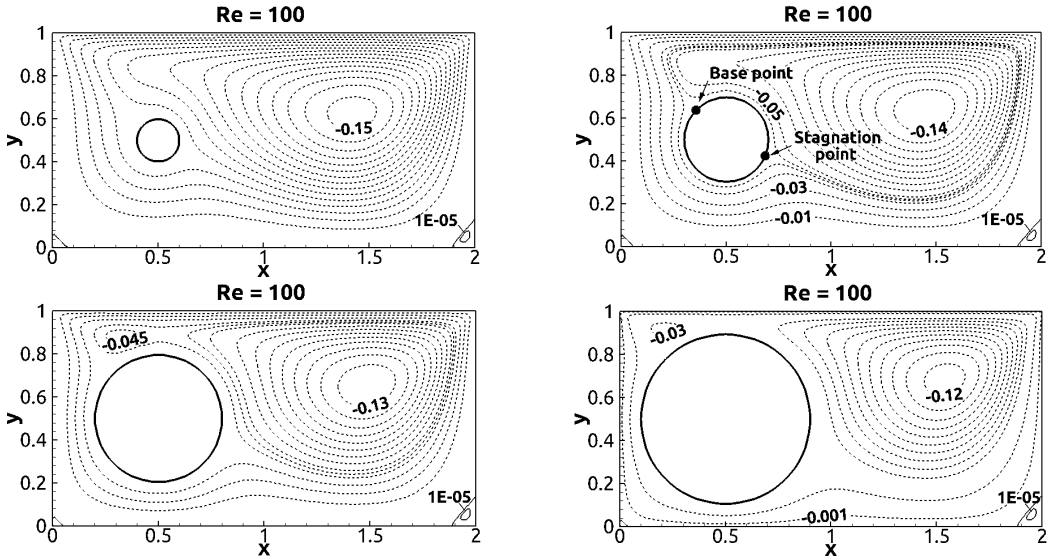

FIG. 7. Streamline contours for flow in a steady lid-driven cavity of AR = 1:2 containing a left-centered cylinder with r = 0.1, 0.2, 0.3 and 0.4 for Re = 100

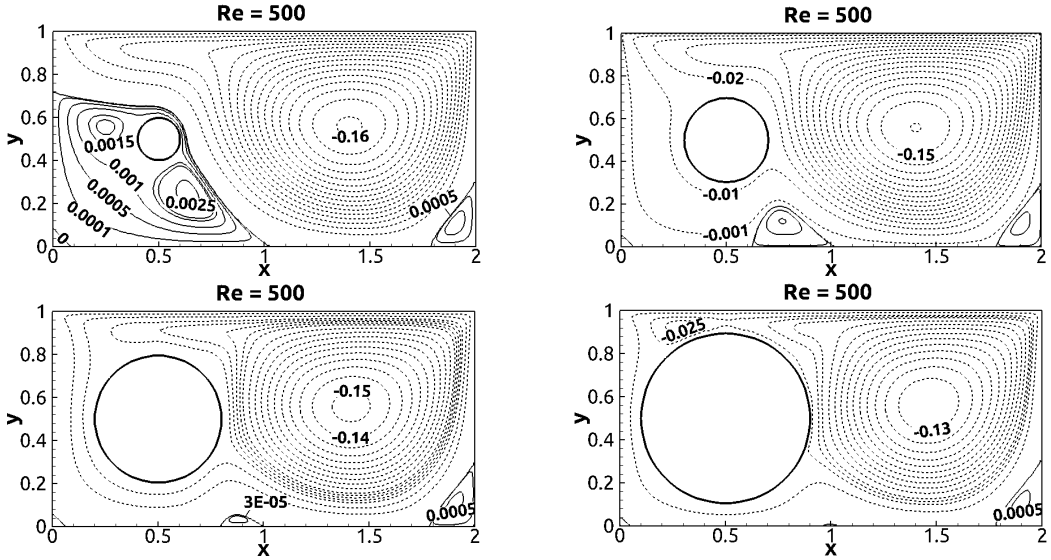

FIG. 8. Streamline contours for flow in a steady lid-driven cavity of AR = 1:2 containing a left-centered cylinder with r = 0.1, 0.2, 0.3 and 0.4 for Re = 500.

Figure 9 shows streamline contours for the same geometry as figures 7 and 8 for Re = 1000. For r = 0.1, a larger anti-clockwise circulation region than for Re = 500 (figure 8) is formed around the cylinder while a large clockwise primary vortex exists to the right of the cylinder. It appears that within the anti-clockwise circulation region, an anti-clockwise vortex is formed at the upper left side of the cylinder while the anti-clockwise vortex formed at the lower right side of the cylinder for Re = 500 (figure 8; r = 0.1) does not exist here due to the increasing size of the circulation region. This flow pattern is denoted V. As r increases to 0.2, the flow exhibits pattern V but with a smaller and weaker anti-clockwise vortex attached to the cylinder than for r = 0.1. For r = 0.3,

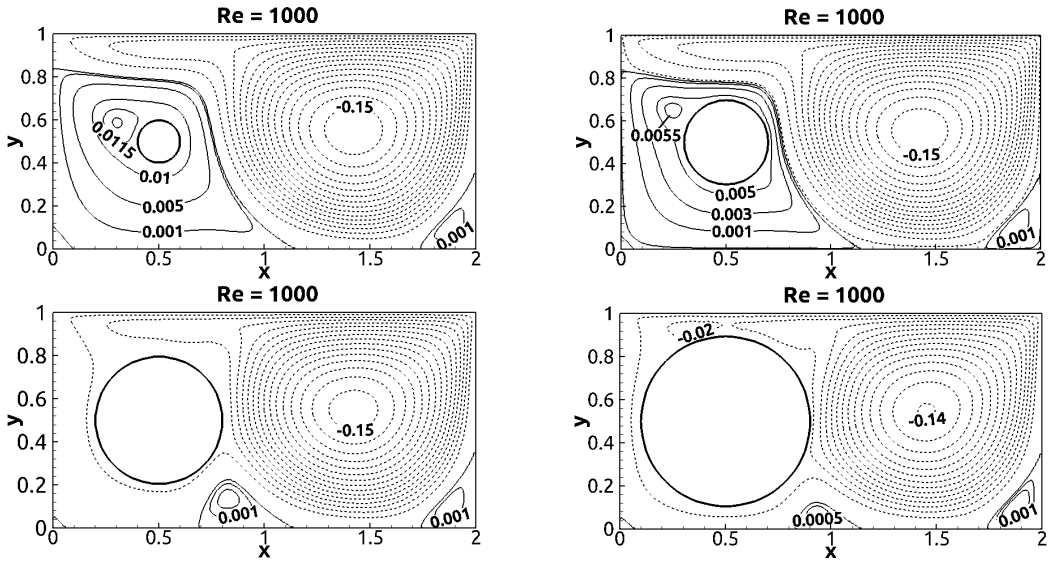

FIG. 9. Streamline contours for flow in a steady lid-driven cavity of AR = 1:2 containing a left-centered cylinder with r = 0.1, 0.2, 0.3 and 0.4 for Re = 1000.

the flow exhibits pattern IV but with a larger and stronger bottom vortex than for Re = 500 (figure 8). As r increases further to 0.4, the bottom vortex remains and a clockwise vortex, which also appears in flow pattern II (figure 7 for r = 0.3 and 0.4), is formed at the upper left side of cylinder. This flow pattern is denoted VI.

2. Centered cylinder

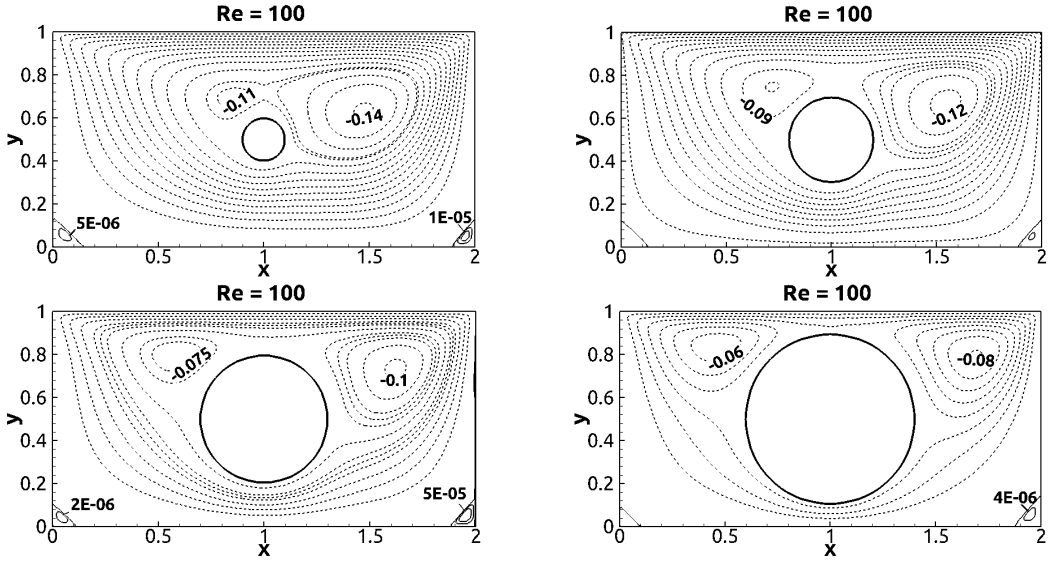

FIG. 10. Streamline contours for flow in a steady lid-driven cavity of AR = 1:2 containing a centered cylinder with r = 0.1, 0.2, 0.3 and 0.4 for Re = 100.

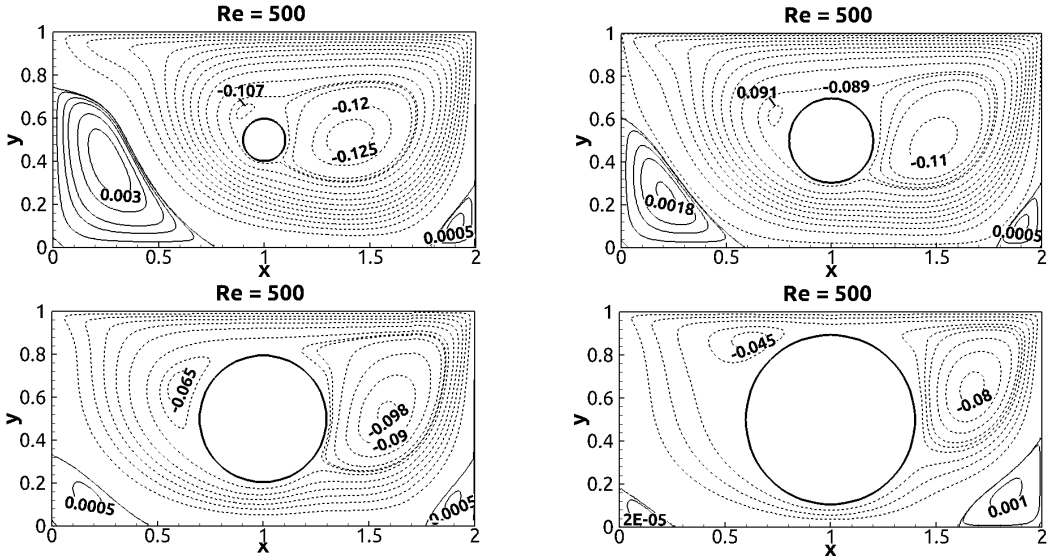

FIG. 11. Streamline contours for flow in a steady lid-driven cavity of AR = 1:2 containing a centered cylinder with r = 0.1, 0.2, 0.3 and 0.4 for Re = 500.

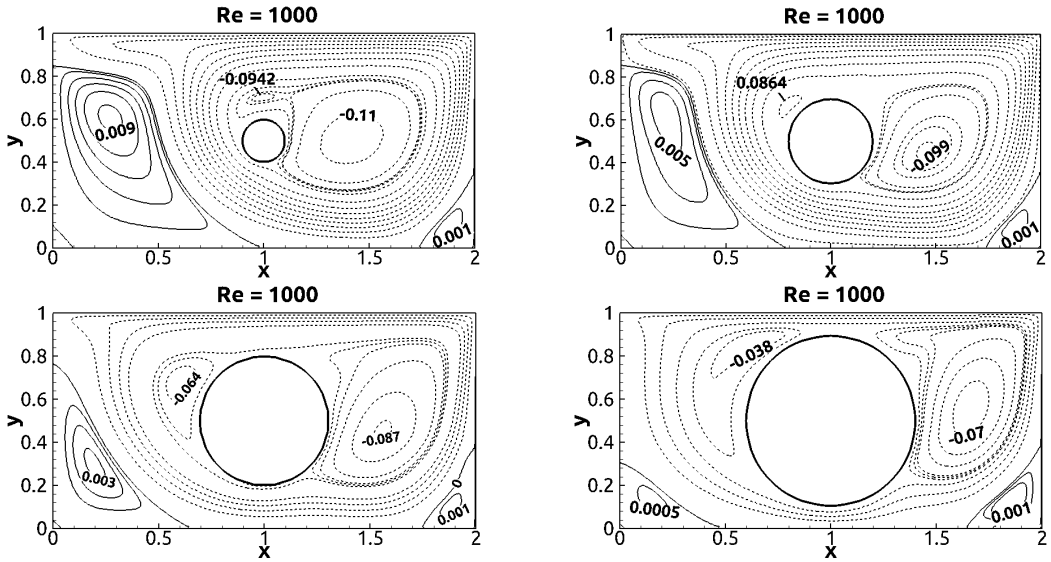

FIG. 12. Streamline contours for flow in a steady lid-driven cavity of AR = 1:2 containing a centered cylinder with r = 0.1, 0.2, 0.3 and 0.4 for Re = 1000.

Figure 10 shows streamline contours for the centered cylinder located at (1, 0.5) for Re = 100 and r = 0.1, 0.2, 0.3 and 0.4. The flow exhibits pattern *II* for all values of r but the clockwise vortex to the left of the cylinder is larger than for the left-centered cylinder (figure 7 for r = 0.3 and 0.4). Young et al.[26] investigated creeping flow for a steady lid-driven rectangular cavity containing a centered rotating and non-rotating cylinder. Two equal clockwise vortices attached to the upper left and right side of the cylinder were formed for the non-rotating cylinder. In the present case, however, the non-linearity of the convective term results in asymmetry of these vortices with the vortex to the right of the cylinder being significantly larger than that to the left of the cylinder. As

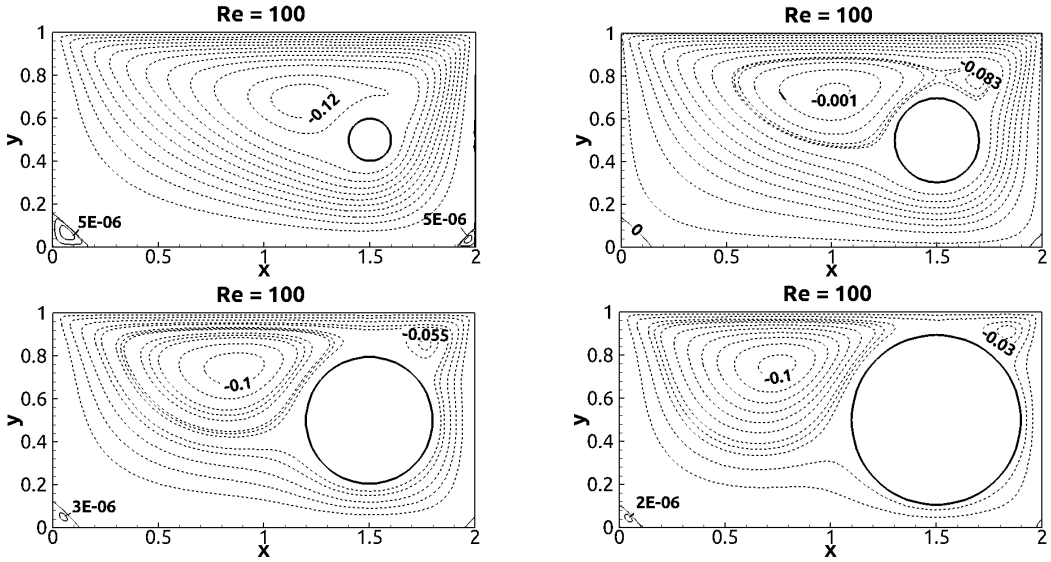

FIG. 13. Streamline contours for flow in a steady lid-driven cavity of AR = 1:2 containing a right-centered cylinder with r = 0.1, 0.2, 0.3 and 0.4 for Re = 100.

r increases, the left clockwise vortex grows gradually in size due to more flow rolling down from the lid at the upper left side of the cylinder. Moreover, it appears that the maxima of the stream function for the left and right clockwise vortices decrease as r increases while the bottom corner vortices are only weakly affected by the cylinder size.

Figures 11 and 12 show streamline contours for the same geometry as shown in figure 10 but for Re = 500 and 1000, respectively. The flow exhibits pattern II for all values of r and Re but with an amplification of the bottom corner vortices due to the higher Reynolds number, which also leads to a weaker clockwise vortex pair attached to the cylinder, as well as the vortex to the left of the cylinder being larger relative to the vortex to the left of the cylinder. As Re increases the vortex to the right of the cylinder moves towards the bottom. Moreover, an increase in r leads to a decay of the bottom left corner vortex while the bottom right vortex is only weakly affected.

3. Right-centered cylinder

Figure 13 shows streamline contours for the cylinder located at (1.5, 0.5) with Re = 100 and r = 0.1, 0.2, 0.3 and 0.4. For r = 0.1, the cavity contains one clockwise vortex to the upper left side of the cylinder and two bottom corner vortices; this flow is denoted flow pattern VII. For r = 0.2, 0.3 and 0.4, a clockwise vortex is also formed at the upper right side of the cylinder; here the flow exhibits pattern II.

Figures 14 and 15 show the streamline contours for Re = 500 and 1000, respectively, for the same geometry as in figure 13. An increase in Re (for a given r) causes the bottom corner vortices to grow, while an increase of r (for a given Re) leads to a decay of the bottom corner vortices. For r = 0.1, the flow exhibits pattern VII both for Re = 500 and 1000 but with a smaller clockwise vortex to the left of the cylinder than for Re = 100 (figure 13). For r = 0.2, the flow exhibits pattern II for Re = 500 with smaller clockwise vortices attached to the cylinder than for Re = 100 while

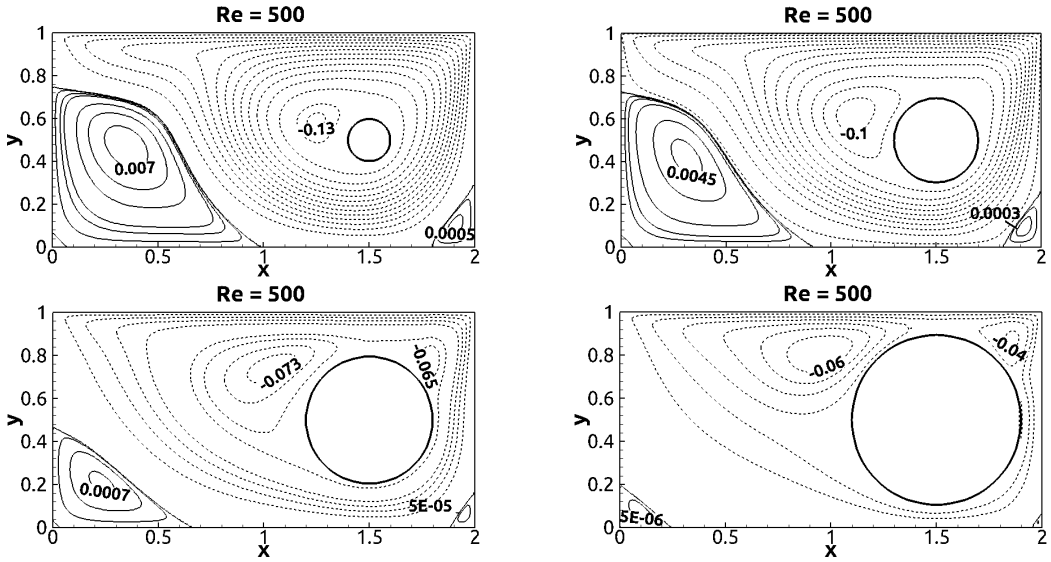

FIG. 14. Streamline contours for flow in a steady lid-driven cavity of AR = 1:2 containing a right-centered cylinder with r = 0.1, 0.2, 0.3 and 0.4 for Re = 500.

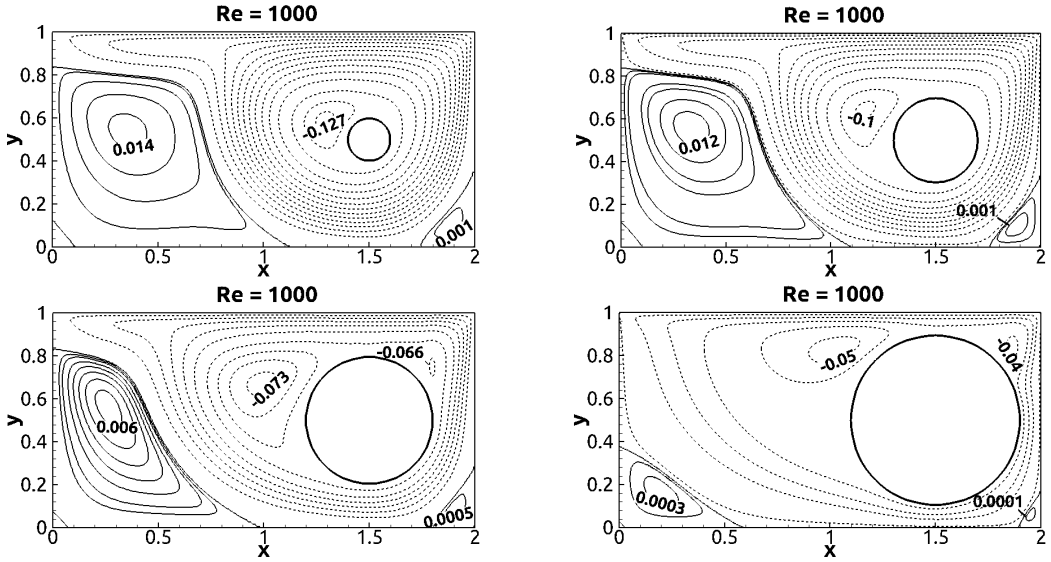

FIG. 15. Streamline contours for flow in a steady lid-driven cavity of AR = 1:2 containing a right-centered cylinder with r = 0.1, 0.2, 0.3 and 0.4 for Re = 1000.

for Re = 1000 the flow exhibits pattern VII. For r = 0.3 and 0.4, the flow exhibits pattern II both for Re = 500 and 1000.

4. Distribution of flow patterns

Figure 16 shows the distribution of flow patterns within the steady lid-driven cavity of AR = 1:2 containing a left-centered (top image) and right-centered (bottom image) cylinder. For the centered

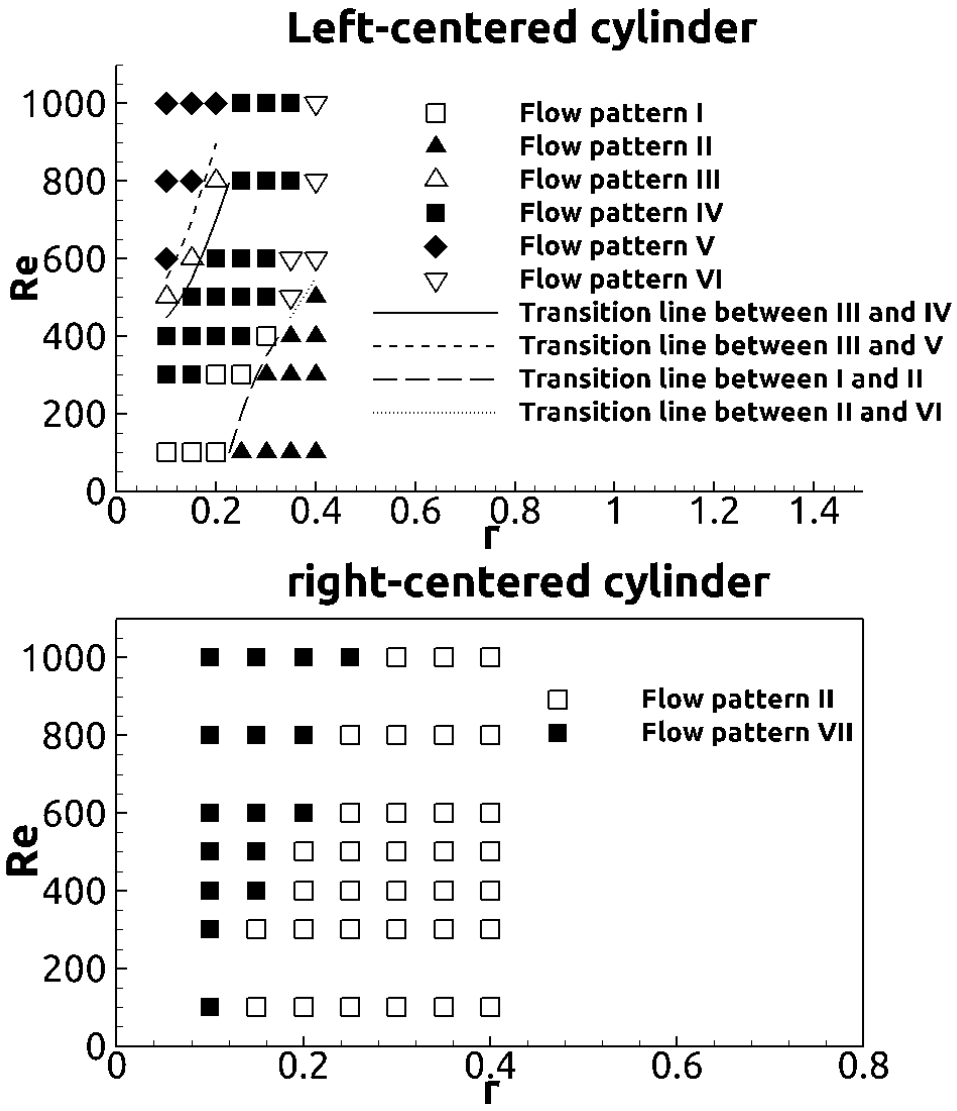

FIG. 16. Distribution of flow patterns within the steady lid-driven cavity of AR = 1:2 containing a left-centered (top image) and right-centered (bottom image) cylinder.

cylinder, only flow pattern II exists (and hence this distribution is not plotted here). The cavity flow with a left-centered cylinder exhibits all the flow patterns, depending on Re and r, except flow pattern VII. This is due to the large anti-clockwise circulation flow formed at the bottom left corner (which also exists in the absence of the cylinder), which here is strongly affected by r and Re. For a given r, there is a tendency that there are more transitions between different flow patterns for small r than for large r (for Re ranging from 100 to 1000) while for a given Re, the number of transitions is larger for high Re than for low Re (for r ranging from 0.1 to 0.4). Figure 16 also shows which transitions are possible. For example, flow pattern V can only have transition to flow pattern III (by either increasing r or decreasing Re), while flow pattern IV can have transition to flow pattern I (by either increasing r or decreasing Re), to flow pattern III (by either decreasing r or increasing Re) and to flow pattern VI (by increasing r). For the right-centered cylinder (bottom image of figure 16), only one new flow pattern VII is formed for relatively small r. An increase of

r leads to a clockwise vortex to the right of the cylinder (forming flow pattern II). To compensate this effect, a higher Re is required to maintain flow pattern VII.

The solid lines in figure 16 denote the transition lines between two different flow patterns. These lines can be given in the form of functional relationships between r and Re as follows:

$$Re = 10955 \times r^2 - 771.36 \times r + 417.96, \qquad III \leftrightarrow IV$$
$$Re = 10000 \times r^2 + 500 \times r + 400, \qquad III \leftrightarrow V$$
$$Re = -13333 \times r^2 + 10333 \times r - 1550, \qquad I \leftrightarrow II$$
$$Re = 2000 \times r - 250, \qquad II \leftrightarrow VI$$

5. Pressure distribution around the cylinder

In the present work, the pressure at the bottom left corner (p_0) is taken as a reference point. The pressure coefficient around the cylinder is given by

$$C_p = \frac{p - p_0}{\frac{1}{2}\rho U^2} \tag{9}$$

where p is the pressure around the cylinder.

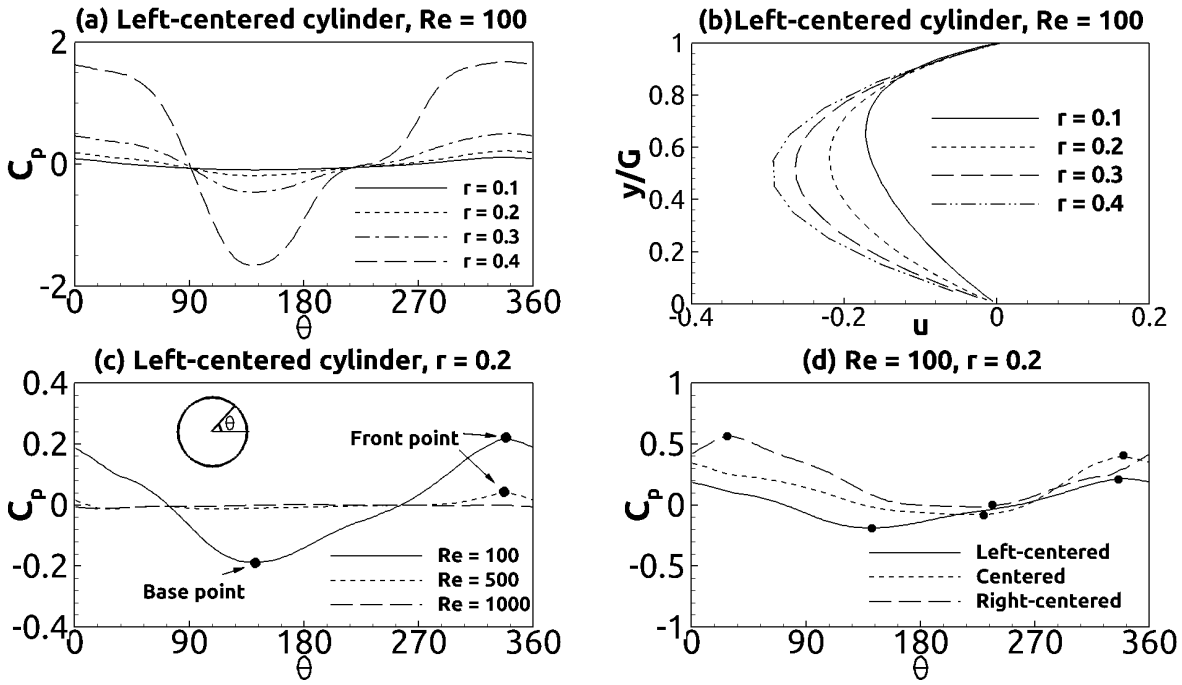

FIG. 17. (a) pressure coefficient C_p around the left-centered cylinder with r = 0.1, 0.2, 0.3 and 0.4 for Re = 100; (b) horizontal velocity $u(0.5, y)$ along the gap between the bottom wall and the cylinder bottom for r = 0.1 0.1, 0.2, 0.3 and 0.4 with Re = 100; (c) C_p around the left-centered cylinder with r = 0.2 for Re = 100, 500 and 1000; (d) C_p around the left-centered, centered and right-centered cylinder with r = 0.2 for Re = 100.

Figure 17 (a) shows the pressure coefficient C_p around left-centered cylinders for four different radii (r = 0.1, 0.2, 0.3 and 0.4) for Re = 100. As r increases, C_p increases. This might be explained by that an increase of r leads to an increase of the gap flow velocity between the cylinder and its adjacent walls (since the gap decreases) as plotted in figure 17 (b), which shows $u(0.5, y)$ along the gap G between the cylinder bottom and the bottom wall for r = 0.1, 0.2, 0.3 and 0.4 with Re = 100.

Figure 17 (c) shows C_p around the left-centered cylinder with r = 0.2 for Re = 100, 500 and 1000. For Re = 100, the base stagnation pressure (i.e., C_p at the base point) and the front stagnation pressure (i.e., C_p at the stagnation point) are consistent with the observation elaborated in figure 7. As Re increases to 500, C_p decreases significantly since the flow velocity around the cylinder decreases as visualized by the streamline contours in figures 7 and 8. For Re = 1000, C_p decreases further and the front stagnation pressure disappears. This is consistent with the observation that the fluid moves anti-clockwise around the cylinder as shown in figure 9.

Figure 17 (d) shows C_p around the left-centered, centered and right-centered cylinders with r = 0.2 for Re = 100. As the cylinder moves towards the right wall, the front and back stagnation points move clock-wise around the cylinder, and the pressure increases since the pressure is larger in the right part of the cavity than in the left part.

IV. SUMMARY AND CONCLUSIONS

A detailed investigation of the flow patterns in the steady lid-driven cavity of depth to width ratio 1:2 containing a circular cylinder of different radii and positions is provided. Here the Reynolds numbers are 100, 500 and 1000 whilst the radii are 0.1, 0.2, 0.3 and 0.4. The positions of the cylinder are left-centered, centered and right-centered. It appears that this flow can be classified into seven different flow patterns visualized by streamline contours. The flow pattern I is composed of one clockwise vortex to the right side of the cylinder and two bottom corner vortices; flow pattern II is composed by two clockwise vortices attached to the left and right side of the cylinder as well as two bottom corner vortices; flow pattern III contains two anti-clockwise vortices attached to the upper left and bottom right sides of the cylinder, a clockwise vortex at the upper right side of the cylinder as well as a bottom right corner vortex; flow patterns IV and VI are composed by flow patterns I and II, respectively, with an additional bottom vortex; flow pattern V is characterized by the anti-clockwise vortex at the lower right side of the cylinder vanishing from flow pattern III; flow pattern VII is characterized by the clockwise vortex to the right of the cylinder vanishing from flow pattern II.

These flow patterns are given for different cylinder radii and positions as well as Reynolds numbers. There is a tendency that for a given cylinder radius, there are more transitions between different flow patterns for a small radius than for a large radius (for Reynolds numbers ranging from 100 to 1000) while for a given Reynolds number, the number of transitions is larger for high Reynolds numbers than for low Reynolds numbers (for radii ranging from 0.1 to 0.4). Overall, a larger number of flow patterns tend to emerge as the Reynolds number increases for small cylinder radii. The largest variety of flow patterns occur for the left-centered cylinder due to the interaction with the large anti-clockwise circulation flow formed at the bottom left corner.

ACKNOWLEDGEMENTS

We gratefully acknowledge the support for this research from the Department of Marine Technology, Norwegian University of Science and Technology and the China Scholarship Council (Grant no. 201506680058).

REFERENCES

[1]H. F. Oztop, Z. Zhao, and B. Yu, "Fluid flow due to combined convection in lid-driven enclosure having a circular body," International Journal of Heat and Fluid Flow **30**, 886–901 (2009).

[2]K. Khanafer and S. Aithal, "Laminar mixed convection flow and heat transfer characteristics in a lid driven cavity with a circular cylinder," International Journal of Heat and Mass Transfer **66**, 200–209 (2013).

[3]A. W. Islam, M. A. Sharif, and E. S. Carlson, "Mixed convection in a lid driven square cavity with an isothermally heated square blockage inside," International Journal of Heat and Mass Transfer **55**, 5244–5255 (2012).

[4]M. Billah, M. Rahman, U. M. Sharif, N. Rahim, R. Saidur, and M. Hasanuzzaman, "Numerical analysis of fluid flow due to mixed convection in a lid-driven cavity having a heated circular hollow cylinder," International Communications in Heat and Mass Transfer **38**, 1093–1103 (2011).

[5]O. Galaktionov, V. Meleshko, G. Peters, and H. Meijer, "Stokes flow in a rectangular cavity with a cylinder," Fluid Dynamics Research **24**, 81 (1999).

[6]K. Khanafer, S. Aithal, M. E. Assad, and I. Pop, "Flow and heat transfer in a driven cavity with two cylinders," Journal of Thermophysics and Heat Transfer **31**, 99–108 (2017).

[7]D. Chatterjee and S. K. Gupta, "Hydromagnetic mixed convective transport in a nonisothermally heated lid-driven square enclosure including a heat-conducting circular cylinder," Industrial & Engineering Chemistry Research **53**, 19775–19787 (2014).

[8]S. Ray and D. Chatterjee, "Mhd mixed convection in a lid-driven cavity including heat conducting circular solid object and corner heaters with joule heating," International Communications in Heat and Mass Transfer **57**, 200–207 (2014).

[9]D. Chatterjee, S. K. Gupta, and B. Mondal, "Mixed convective transport in a lid-driven cavity containing a nanofluid and a rotating circular cylinder at the center," International Communications in Heat and Mass Transfer **56**, 71–78 (2014).

[10]S. Bansal and D. Chatterjee, "Magneto-convective transport of nanofluid in a vertical lid-driven cavity including a heat-conducting rotating circular cylinder," Numerical Heat Transfer, Part A: Applications **68**, 411–431 (2015).

[11]D. Chatterjee and P. Halder, "Magnetoconvective transport in a lid-driven square enclosure with two rotating circular cylinders," Heat Transfer Engineering **37**, 198–209 (2016).

[12]E. Fadlun, R. Verzicco, P. Orlandi, and J. Mohd-Yusof, "Combined immersed-boundary finite-difference methods for three-dimensional complex flow simulations," Journal of Computational Physics **161**, 35–60 (2000).

[13]N. Peller, A. L. Duc, F. Tremblay, and M. Manhart, "High-order stable interpolations for immersed boundary methods," International Journal for Numerical Methods in Fluids **52**, 1175–1193 (2006).

[14]P. A. Berthelsen and O. M. Faltinsen, "A local directional ghost cell approach for incompressible viscous flow problems with irregular boundaries," Journal of Computational Physics **227**, 4354–4397 (2008).
[15]Y.-H. Tseng and J. H. Ferziger, "A ghost-cell immersed boundary method for flow in complex geometry," Journal of Computational Physics **192**, 593–623 (2003).
[16]M. Coutanceau and R. Bouard, "Experimental determination of the main features of the viscous flow in the wake of a circular cylinder in uniform translation. part 1. steady flow," Journal of Fluid Mechanics **79**, 231–256 (1977).
[17]F. Bouchon, T. Dubois, and N. James, "A second-order cut-cell method for the numerical simulation of 2D flows past obstacles," Computers & Fluids **65**, 80–91 (2012).
[18]R. Gautier, D. Biau, and E. Lamballais, "A reference solution of the flow over a circular cylinder at Re= 40," Computers & Fluids **75**, 103–111 (2013).
[19]B. Fornberg, "A numerical study of steady viscous flow past a circular cylinder," Journal of Fluid Mechanics **98**, 819–855 (1980).
[20]D. V. Patil and K. Lakshmisha, "Finite volume TVD formulation of lattice Boltzmann simulation on unstructured mesh," Journal of Computational Physics **228**, 5262–5279 (2009).
[21]A. S. Grove, F. Shair, and E. Petersen, "An experimental investigation of the steady separated flow past a circular cylinder," Journal of Fluid Mechanics **19**, 60–80 (1964).
[22]S. Dennis and G.-Z. Chang, "Numerical solutions for steady flow past a circular cylinder at Reynolds numbers up to 100," Journal of Fluid Mechanics **42**, 471–489 (1970).
[23]S.-G. Cai, A. Ouahsine, J. Favier, and Y. Hoarau, "Moving immersed boundary method," International Journal for Numerical Methods in Fluids **85**, 288–323 (2017).
[24]M. Cheng and K. Hung, "Vortex structure of steady flow in a rectangular cavity," Computers & Fluids **35**, 1046–1062 (2006).
[25]J. Zhu, L. E. Holmedal, H. Wang, and D. Myrhaug, "Vortex dynamics and flow patterns in a two-dimensional oscillatory lid-driven rectangular cavity," European Journal of Mechanics-B/Fluids (2019).
[26]D. Young, C. Chen, C. Fan, K. Murugesan, and C. Tsai, "The method of fundamental solutions for stokes flow in a rectangular cavity with cylinders," European Journal of Mechanics-B/Fluids **24**, 703–716 (2005).